2012-12-08

Comparing Theory and Experiment for Analyte Transport in the First Vacuum Stage of the Inductively Coupled Plasma Mass Spectrometer

Matthew R. Zachreson
Brigham Young University - Provo

Comparing Theory and Experiment for Analyte Transport in the First Vacuum Stage of the Inductively Coupled Plasma Mass Spectrometer

Matthew R. Zachreson

A thesis submitted to the faculty of
Brigham Young University
in partial fulfillment of the requirements for the degree of

Master of Science

Ross L. Spencer, Chair
Paul B. Farnsworth
Grant W. Hart

Department of Physics and Astronomy

Brigham Young University

December 2012

ABSTRACT

Comparing Theory and Experiment for Analyte Transport in the First Vacuum Stage of the Inductively Coupled Plasma Mass Spectrometer

Matthew R. Zachreson
Department of Physics and Astronomy, BYU
Master of Science

The Direct Simulation Monte Carlo algorithm as coded in FENIX is used to model the transport of trace ions in the first vacuum stage of the inductively coupled plasma mass spectrometer. Haibin Ma of the Farnsworth group at Brigham Young University measured two radial trace density profiles: one 0.7 mm upstream of the sampling cone and the other 10 mm downstream. We compare simulation results from FENIX with the experimental results. We find that gas dynamic convection and diffusion are unable to account for the experimentally-measured profile changes from upstream to downstream. Including discharge quenching and ambipolar electric fields, however, makes it possible to account for the way the profiles change.

Keywords: inductively coupled plasma mass spectrometry, gas flow simulation, direct-simulation Monte Carlo, DSMC

ACKNOWLEDGMENTS

I would like to thank my advisor, Dr. Ross Spencer, for the countless hours that he has dedicated to helping me conduct good research, debugging code, expanding my understanding of physics, and editing this thesis.

I would also like to thank David Oliphant for guiding me in my first real research efforts as an undergraduate and inspiring me to continue on to graduate studies.

Lastly, I would also like to thank my wife who has provided me with endless support and encouragement.

Contents

List of Figures

List of Tables

Chapter 1

Introduction

A jet freely expanding into a vacuum was first described by Owen and Thornhill (1). Ashkenas and Sherman expanded the work of Owen and Thornhill and others and created an exhaustive fluid model of the expansion. (2) (see Fig. 1.1) This model is limited in the fact that it was created using inviscid flow theory. Inviscid flow theory is invalid when the mean free path is $\sim$0.1% of a characteristic distance of the flow, such as the nozzle radius, since inviscid flow theory assumes that the mean free path is very small compared to the features of flow being described. It also ignores boundary layers, which are viscous effects.

To make a more accurate model, Brook and Oman (3) applied the Boltzmann equation to the problem using the BGK method. (4) Later, Hamel and Willis (5) created a better approximation to the Boltzmann equation by using the hypersonic approximation. Knuth and Fisher (6) were able to get past the hypersonic approximation by assuming a single temperature Maxwell-Boltzmann velocity distribution in the expansion. Miller and Andres extended this model using classical scattering theory (7) and Toennies and Winklemann were able to improve it further considering the temperature perpendicular to the flow and the temperature parallel to the flow separately. (8) Toennies and Winklemann's resulting model is more accurate than the fluid model, but is much more cumbersome to use.

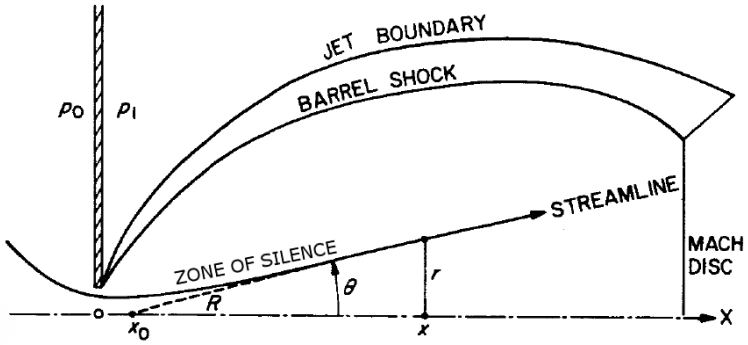

Figure 1.1 Diagram of a “free jet" expansion taken from Ashkenas and Sherman.(2). Gas is allowed to rapidly expand through a small hole in the boundary between a high pressure p_0 region to a much lower pressure p_1 region. If the pressure difference is great enough, the flow velocities through the hole exceed the speed of sound, and the steady-state “free jet" is formed. This high speed region is called the zone of silence because sound waves cannot propagate upstream. A shock forms at the edge of the expansion where the rapidly expanding gas interacts with the stationary background gas. The result is a rapid decrease in the fluid velocities and an increase in the temperature and density of the gas across the barrel and the mach disc shock as the pressure in the expanding gas increases to match the background pressure.

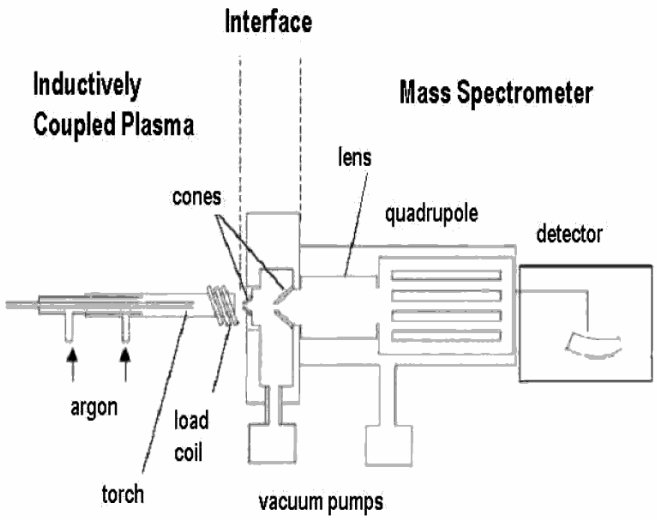

Figure 1.2 Schematic of an ICP-MS. Taken from Somers(11)

Modeling the free jet expansion is important because the expansion is an excellent molecular beam source. (9; 10) It is an essential part of the ion beam formation in an inductively coupled plasma mass spectrometer (ICP-MS). The ICP-MS (see Fig. 1.2) injects samples to be analyzed into an argon torch which is at a temperature of 8000 K. The now ionized sample and the background argon then enter into a vacuum stage through the sampling cone, where they undergo a free jet expansion. The center of the jet continues through a skimmer cone to create a rough ion beam, which is then focused with an ion lens. An electric quadrupole then sorts the focused ion beam by the particles' charge to mass ratio. Then the particles are detected and the sample is analyzed. The IPC-MS can detect up to sub-ppt.

Douglas and French were the first to model the free jet expansion through the sampling cone of an ICP-MS (12; 13) They applied the fluid methods of Ashkenas and Sherman directly to the argon flow in the ICP-MS and created their hemispherical sink model.

Later, Spencer et al. created a better approximation to the argon flow in the ICP-MS based on data from the direct simulation Monte Carlo (DSMC) code FENIX. (14; 15; 16) Not only is FENIX more accurate than the fluid models, but it is more robust than the Boltzmann equation

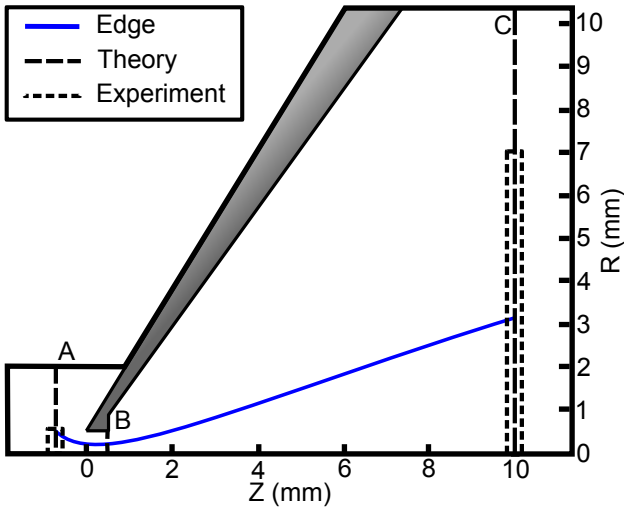

Figure 1.3 Region simulated by FENIX. Experiment denotes the areas averaged over when taking the experimental data. (18) Theory denotes where the theoretical profile starts (labeled A), is passed from one geometry to the next (labeled B), then where it ends (labeled C). Edge shows where the ideal fluid equations map the outer edge of the upstream experimental profile from upstream to downstream.

models.

In order to understand the ICP-MS, it is not enough to study just the argon flow, but also the behavior of the analyte ions entrained in the flow. In an effort to better understand the analyte behavior, the FENIX code has been expanded to simulate analyte flow as well. The FENIX analyte simulation matches upstream barium data collected by Macedone et al.(17) and shows that the axial analyte density drop seen in Macedone's data is a result of diffusion. A second model, the continuity equation solver ProfileMapper, has also been developed and it agrees with FENIX analyte output. The models are compared to calcium and barium density profiles imaged by Haibin Ma in two regions: one 0.7 mm upstream of the sampling cone and another 10 mm downstream from the sampling cone (18). (See Fig. 1.3) FENIX and ProfileMapper produce results that agree with each other, but they do not agree with the experimental data. However, adding electron-ion recombination and ambipolar field effects to the models allows the models to match the experimental data.

Chapter 2

Theoretical

Spencer et al. have already given the details on how FENIX works for argon flow (14). We simulate analyte flow by adding trace particles to FENIX and also by using a continuity equation solver named ProfileMapper.

2.1 FENIX- analyte addition

The added simulation trace particles follow the same three basic steps that the argon particles follow:

1. FENIX advances each particle from time step n to time step $n+1$ through:

$$\mathbf{x}_{n+1} = \mathbf{x}_n + \mathbf{v}_n \tau, \quad \mathbf{v}_{n+1} = \mathbf{v}_n, \tag{2.1}$$

   where $\mathbf{x}$ is the particle position, τ is the time step, and $\mathbf{v}$ is the particle velocity.

2. FENIX assigns each particle to a collision cell.

3. FENIX gives each particle a random chance to collide with the nearest argon neighbor in its collision cell using the collision statistics appropriate to the density and temperature in

the cell (19). Analyte densities are too small to have good statistics when the argon-analyte density ratio is preserved, and simply increasing the number of simulation argon particles to obtain good analyte statistics is computationally expensive. To correct this problem, two assumptions are made that make it possible to use about the same number of simulation trace particles as simulation argon particles even though their densities are vastly different. First, the fact that analyte-argon collisions dominate over analyte-analyte collisions is used. This is done by only allowing simulation trace particles to collide with simulation argon particles but not with each other. Second, it is assumed that the analyte does not significantly affect the argon flow, so when a simulation trace particle collides with a simulation argon particle, only the trace particle gets a new velocity.

Collisions are simulated with the Variable Soft Sphere (VSS) model of Koura et al. (20; 21). Their collision model is equivalent to a differential cross-section $\sigma(\theta)$ given by (14):

$$\sigma(\theta) = \frac{\alpha A v_r^{-2\nu}}{4\pi} \left[\cos^2(\theta/2)\right]^{\alpha-1}, \tag{2.2}$$

where v_r is the relative speed of the colliding particles and where θ is the center-of-mass scattering angle. A, ν, and α are chosen to fit the collision integral data collected by Ellis et al. (22; 23; 24; 25). They relate to the collision integral $\Omega^{(1,1)}(T)$ through:

$$\Omega^{(1,1)}(T) = \frac{A\Gamma(3-\nu)}{1+\alpha} \left(\frac{m_r}{2k_b}\right)^{\nu} T^{-\nu} \tag{2.3}$$

where T is the temperature, m_r is the reduced mass of the ion and the argon, and k_b is Boltzmann's constant. The data tables of Ellis et al. allow the magnitude, $A/(1+\alpha)$, and the exponent ν to be fitted; therefore, ν can be determined directly, but only the ratio $A/(1+\alpha)$ can be determined, not A and α separately. Since α generally falls between 1 and 2.5 (20; 21), as a test simulations were run with three values of α: 1, 1.66, and 2 along with the corresponding values of A. The three results differed by less than 1%. The value $\alpha = 1.66$ is chosen simply because it corresponds to the best value of α to use for argon-argon collisions (14).

Ellis et al. collected Ba^+ transport data only up to 2500 K. However, the ICP reaches temperatures near 5000 K. However, they did collect data for Cs^+ up to 10000 K. A two power fit was made to the collision integral data for Cs^+:

$$\Omega^{(1,1)}(T) = 3.8697 \times 10^3 T^{-.6616} + .4469 T^{.3289}$$

This two power fit was chosen because it fit the data well. Cesium was chosen because it is in the same periodic group as barium. To create an estimate for the high temperature Ba^+ collision integral, the extra fitting parameters $\eta,\ \gamma,\ \beta$ were added:

$$\Omega^{(1,1)}(T) = \eta \left[3.8697 \times 10^3 \left(T^\gamma + \beta\right)^{-.6616} + .4469 \left(T^\gamma + \beta\right)^{.3289} \right]$$

and were determined by doing a least squares fit to the available Ba^+ collision integral data. This resulted in values of $\eta = .9181,\ \gamma = .7292$ and $\beta = 42.21$. To test the accuracy of the predicted high temperature collision integral for Ba^+, $\eta,\ \gamma$, and β were found for several ions that have high temperature collision integral data available. The fitting parameters were determined only using data below 2500 K, and then the fit results were compared to the higher temperature experimental data. This method predicts the collision integral data for K^+ and Rb^+ up to 12000 K within 1.5% and predicts Na^+ and O^+ up to 6000 K within 5%. Therefore, the predicted Ba^+ collision integral values should also be accurate within a few percent.

Ellis et al. collected no Ca^+ data. To estimate the Ca^+ collision integral, the $\eta,\ \gamma,\ \beta$ needed to scale Cs^+ to K^+ are found then applied to a two power fit to the extrapolated Ba^+ data. Since cesium and potassium share the same relationship in the periodic table as barium and calcium, this should provide a reasonable estimate of the Ca^+ collision integral as a function of temperature.

The single power of temperature used by Eq. (2.3) does not fit well over a large temperature range. To still use the VSS model, ν is fitted only over the temperature range present in the

	ν	$A\ (m^{2(\nu+1)}/s^{2\nu})$	T. Range (K)
Ca^+ upstream	0.536	1.335×10^{-14}	1500-6000
Ca^+ downstream	0.815	7.149×10^{-14}	100-2500
Ba^+ upstream	.488	5.532×10^{-16}	1500-6000
Ba^+ downstream	.681	8.483×10^{-15}	100-2500

Table 2.1 The values of ν and A used in the FENIX simulation and the temperature ranges over which they are valid.

simulation. Fitting only over the needed temperature data produces different ν values for different simulation regions, but allows the experimental data to be matched within 1% in that region. The resulting values of ν and A can be found in Table 2.1.

To avoid problems created by the large density difference between the high density region upstream of the sampling cone and the low density region downstream, the simulation volume is divided into two smaller regions. (see Fig. 1.3) The first region simulates the volume upstream of the sampling cone, through the sampling cone, and continues on to 1 mm downstream. The flow data at the back edge of the sampling cone are used to seed the second simulation region. This second region includes everything downstream of the sampling cone. The small volume of overlap between the two regions provides an opportunity to make sure that the transition between regions happens correctly.

2.2 ProfileMapper

To validate FENIX's analyte results and to obtain a faster computational model, we wrote another program, ProfileMapper, in MatLab. ProfileMapper is a continuity equation solver. It assumes that the analyte is entrained in the argon flow and then uses the argon velocity data generated by

FENIX to solve the continuity equation with diffusion and gain or loss of analyte:

$$n\nabla\cdot\mathbf{v}+\mathbf{v}\cdot\nabla n=\nabla\cdot(D\nabla n)+S \tag{2.4}$$

where n is the analyte number density, $\mathbf{v}$ is the argon fluid velocity, D is the diffusion coefficient, and S represents any other source or sink terms. This source or sink term makes it possible to include ionization and quenching. Quenching will be addressed quantitatively later.

The simplest form of Eq. (2.4) neglects diffusion and gain or loss and so only describes ideal convection. In this approximation, Eq. (2.4) becomes:

$$n\nabla\cdot\mathbf{v}+v\frac{dn}{ds}=0 \tag{2.5}$$

where ds is distance along the streamlines (see Fig. 2.1) and where v is the magnitude of the velocity. Separating the variables of Eq. (2.5) and integrating along the streamlines gives:

$$n_I(r,z)=n_0(r)\exp\left[-\int\frac{\nabla\cdot\mathbf{v}}{|v|}ds\right] \tag{2.6}$$

where $n_0(r)$ is an initial analyte density profile at a fixed value of z on the FENIX output grid and $n_I(r,z)$ is the resulting ideal analyte density.

If diffusion is added, Eq. (2.5) becomes:

$$n\nabla\cdot\mathbf{v}+\mathbf{v}\cdot\nabla n=\nabla\cdot(D\nabla n) \tag{2.7}$$

Integrating along streamlines as was done in Eq. (2.6) then gives the formal solution:

$$n(r,z)=n_I(r,z)\exp\left[\int\frac{\nabla\cdot(D\nabla n)}{n|v|}ds\right] \tag{2.8}$$

where n is the diffused analyte density and where D is the diffusion coefficient. ProfileMapper treats the diffusive term as a small perturbation and obtains a solution by iterating on Eq. (2.8). The iteration process begins with $n=n_I$, the ideal density from Eq. (2.6), and finishes when $n(r,z)$ satisfies Eq. (2.7).

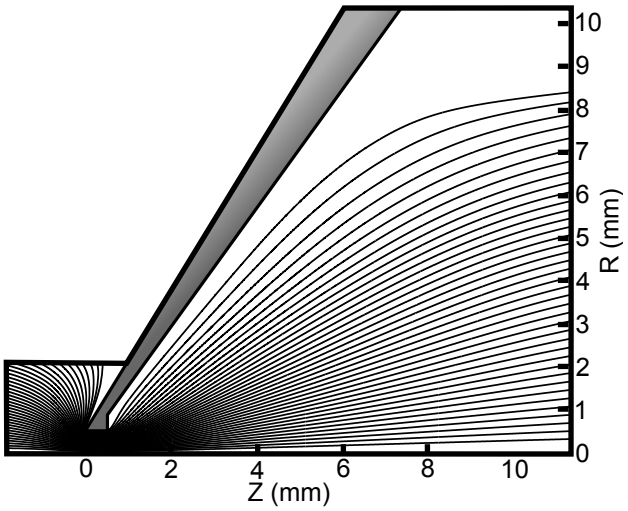

Figure 2.1 Streamlines of the argon flow in the simulated region.

This iteration procedure fails when fluid velocities are low and D is large, which causes the exponential term in Eq. (2.8) to diverge.

The diffusion coefficient is obtained from the mobility data collected by Ellis et al. (22; 23; 24; 25). Their data are converted into a diffusion coefficient using the Einstein relation

$$D = \frac{\mu k_b T}{q} \tag{2.9}$$

where μ is the mobility, k_b is Boltzmann's constant, T is the temperature, and q is the charge of the ion. Since there is no mobility data for calcium, it is estimated using the same method used to estimate the collision integral data. The higher temperature barium mobility data were also extrapolated using cesium mobility data. The results are

$$\mu_{Ba} = \frac{1}{n_{Ar}} \frac{2.686 \times 10^{21} T^{0.349}}{3.554 + 4.249 \times 10^{-3} T^{.837} - 3.58 \times 10^{-3} T^{-.00423}}$$

for barium and

$$\mu_{Ca} = \frac{1}{n_{Ar}} \frac{2.686 \times 10^{21} T^{0.459}}{4.952 + .0131 T^{.789} - 1.311 \times 10^{-3} T^{-.0617}}$$

for calcium in units of $m^2/(V \cdot s)$ with T in Kelvins. n_{Ar} is the argon number density in m^{-3}

Care must be taken in using a diffusion coefficient when the mean free path is large compared to the size of the region being studied. The problem is that diffusion is limited by the largest

possible particle flux; however, with large density gradients $D\nabla n$ can predict faster flow than the thermal particle flux would allow. This means that in order for the diffusion term in Eq. (2.7) to be physical, the diffusion flux Γ must be less than the thermal flux nv_{th}. Γ roughly is given by:

$$\Gamma = D\nabla n \sim \frac{Dn}{L} \tag{2.10}$$

where L is a representative scale length. In the region upstream of the nozzle and in the zone of silence, Γ is less than 5% of nv_{th}. In the shock zone, however, Γ reaches a significantly larger percentage of nv_{th}, but never exceeds half of nv_{th}. However, in this region, the fluid velocity is high enough that diffusion effects are negligible. This means that the drift diffusion equation (Eq. 2.7) should be physical when using velocity data supplied by FENIX.

Chapter 3

Results and discussion

3.1 Comparison of FENIX to upstream data

Mills et al. (17) collected density data for barium atoms and barium ions in the region between the load coil and the sampling cone. Near the load coil, they observed the axial ion densities increase in proportion to the decrease in the barium atom population. However, after reaching a peak value, the barium ion density mysteriously began to drop without an increase in the barium atom density.

To understand the ion density drop, and to validate the FENIX analyte model, FENIX is used to simulate the barium ion population in the same region as the data. FENIX is started at 2 mm upstream of the sampling cone with its initial profile taken from the upstream barium ion data (flow rate = 1.39 L/min.) at that point. 2 mm is chosen because that is where the barium ion population is no longer growing, and therefore no ionization simulation is needed. The results are presented in Fig 3.1. The FENIX results match the experimental data until entering a region where Mills reported signal attenuation. The attenuation could be the result of electron-ion recombination. Convection alone shows an increase in axial barium density. The streamlines squeeze the profile as it enters the sampling cone. The FENIX simulation results show that the axial density drop

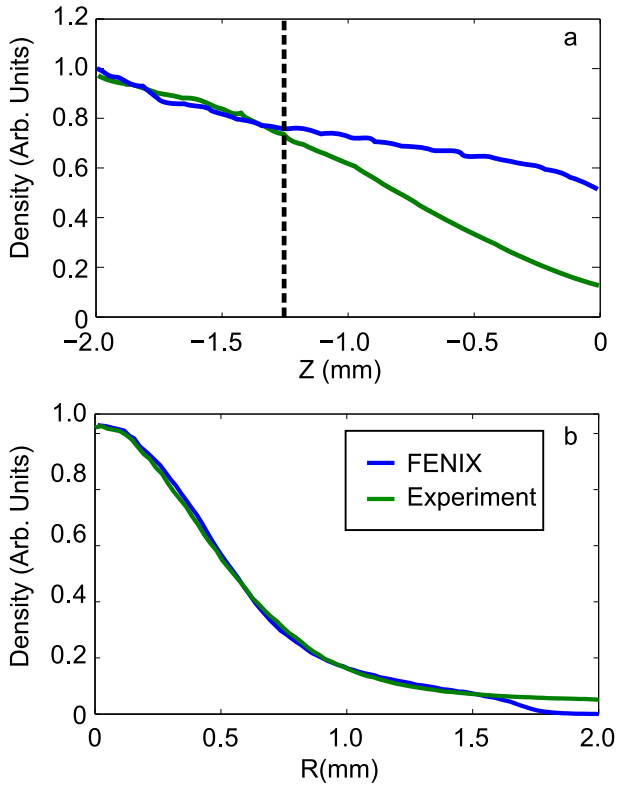

Figure 3.1 Axial (a) and radial (b) ion density profiles taken from FENIX and Mills' experimental data(17). FENIX was started with the experimental profile at Z = -2 mm. Graph (a) shows the ion density along the z-axis at R=0. The drop in ion density comes strictly from diffusion and convection. Graph (b) shows the radial ion density from both FENIX and the experiment at Z= -1.25 mm (The vertical dotted line in graph (a)). Mills reported signal attenuation starting at Z= - 1.0 $\pm$ 0.5 mm, which is the region where the FENIX and experimental axial ion densities disagree.

is a result of diffusion, which explains why Mills et al. saw an axial ion density drop without seeing the atom population increase. From -2.0 mm to -1.25 mm, the full width at half max of the radial barium density profile contracts by 15%, which FENIX is able to reproduce, suggesting that FENIX accurately simulates convection and diffusion.

3.2 The first vacuum stage

To simulate the flow into the first vacuum stage, FENIX and ProfileMapper are first given starting profiles that are fitted to Ma's (18) upstream data at 0.7 mm upstream from the sampling cone. (See Fig. 3.2) These profiles are then propagated to 10 mm downstream using both FENIX and ProfileMapper. During the downstream expansion, both models produce the $1/z^2$ density dependence along the center line predicted by Douglas and French (12; 13) and measured for electrons by Niu and Houk (26).

The densities produced by FENIX and diffusive ProfileMapper agree; therefore, it is reasonable to conclude that they both accurately simulate the gas dynamic convection and diffusion. The profiles produced are also comparable to those collected by Ma, although they are about 25% too wide at 10 mm. Therefore, the standard physical effects of convection, conduction, and diffusion, while close, are insufficient to describe the transition of analyte profiles from 0.7 mm upstream of the sampling cone to 10 mm downstream of the cone. These effects account for all possible effects that conserve ions.

The extra narrowing of profiles must therefore come from a non-ion-number-conserving effect. The most likely candidate is discharge quenching. The data collected by Gamez and Lehn et al. (27) suggest that no significant quenching occurs up to 5 mm upstream of the sampling cone. However, the data collected by Macedone and Farnsworth (28) show that just downstream of the sampling cone more calcium ions are recombining into calcium atoms than atoms are being ionized into ions. (See Fig. 3.3) This net quenching effect dies out once the ions have traveled more than 3 mm downstream of the sampling cone due to the rapid drop in electron density.

Using the non-quenching FENIX output to scale away the density drop due to the expansion of the calcium ion and atom densities allows the ion density decay rate and the atom density growth rate to be calculated. To calculate the rates, the travel time is also needed. FENIX gives the travel time from 1 mm downstream of the sampling cone to 2 mm downstream as $2.9 \pm .1 \mu s$.

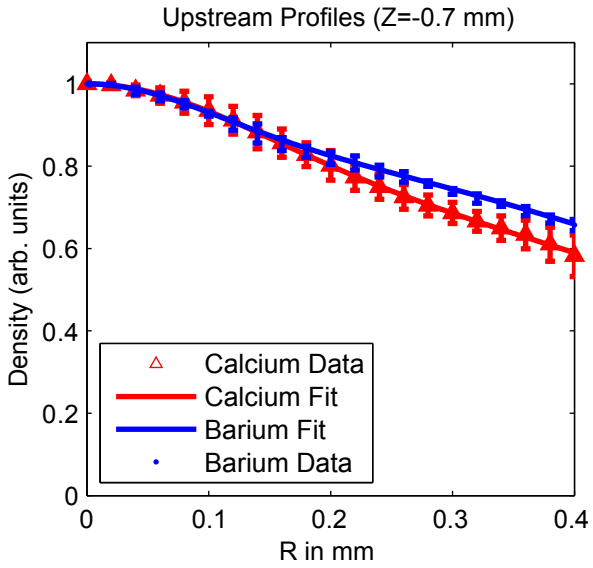

Figure 3.2 The upstream density profiles collected by Ma (18), with their theoretical fits. $n = .8672\exp(-R^2/5.844\times10^{-7}) + .1328\exp(-R^2/1.8770\times10^{-8})$ was used for Ba^+ and $n = .7946\exp(-R^2/5.2717\times10^{-7}) + .2036\exp(-R^2/3.4068\times10^{-8})$ was used for Ca^+. R is in meters and n is normalized to one at $R = 0$.

Assuming exponential growth for the atoms and decay for the ions, and using the time information given by FENIX gives a decay rate of $1.5 \pm .3 \times 10^5 s^{-1}$ for the calcium ions and a growth rate of $1.7 \pm .1 \times 10^5 s^{-1}$ for the calcium atoms in the region from 1 mm to 2 mm downstream of the sampling cone, which roughly agree, meaning that the atom population grows at the same rate as the ion population decays. The estimated error was calculated by applying standard Gaussian error propagation to the reported experimental error.

The potential causes of quenching in this region are three body and radiative recombination. Three body recombination α_3 is orders of magnitude larger than radiative recombination and is given by: (29)

$$\alpha_3 = 8.75\times10^{-27} T_e^{-4.5} \mathrm{cm}^6/\mathrm{s}. \tag{3.1}$$

To convert this rate constant into a rate, it must be multiplied by the electron density squared ${n_e}^2$. Using $n_e = 10^{14}$ cm^{-3}, which is taken from Houk, (26) and the rates taken from Macedone's data(28) into Eq. (3.1) and solving for the electron temperature gives an electron temperature of

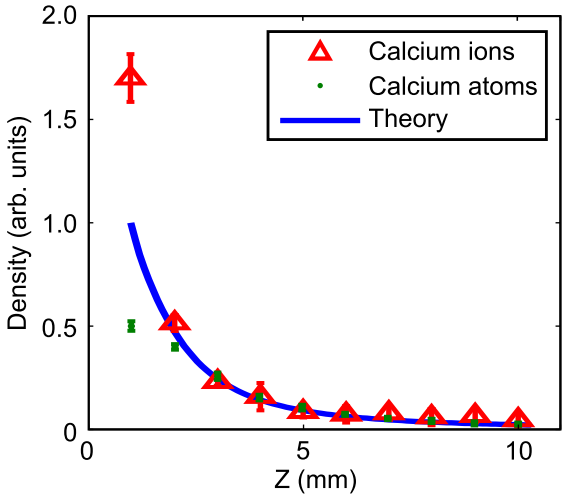

Figure 3.3 Axial variation of calcium ion and calcium atom densities as measured by Macedone and Farnsworth (28) compared to the density predicted by FENIX without recombination. To match the experimental data, the FENIX output was integrated over a 0.5 mm radius cylinder centered about the nozzle axis. From 3 mm downstream of the sampling cone and onward, both the atom and ion densities match the density variation predicted by FENIX. From 1-3 mm downstream of the sampling cone, the ion density decreases more rapidly than predicted by transport theory and the atom density decreases more slowly than predicted by transport theory, suggesting that calcium ions are recombining into calcium atoms until 3 mm downstream of the sampling cone.

$\sim 2500K$ From 1 mm to 2 mm downstream of the sampling cone.

Quenching occurring just upstream of the sampling cone, where Mill's data suggests that there might be quenching, would have a net narrowing effect on the density profiles. In the region from 0.7 mm upstream of the sampling cone to the tip of the sampling cone, the further an ion is from the cone axis, the longer it takes to travel through the region. (See Fig. 3.4) This travel time effect disappears once the flow has entered the sampling cone nozzle, and therefore quenching would no longer have a narrowing effect, and would no longer change the shape of the density profile, but rather only its magnitude.

There is not enough data to accurately model quenching in this region.Upstream quenching rates are difficult to estimate since they depend on n_e^2 and $T_e^{-4.5}$. Small variations in either density

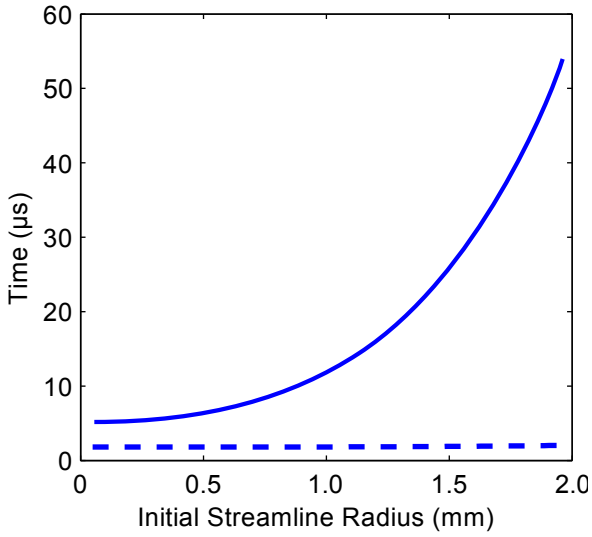

Figure 3.4 Travel time along streamlines as a function of initial streamline radius. Streamlines were started at 0.9 mm upstream of the sampling cone. This location marks the furthest point upstream that was averaged over by Ma to collect the density data. The solid line is the travel time from 0.9 mm upstream from the sampling cone entrance to the entrance. The dotted line shows the travel time from the sampling cone entrance to 3.5 mm downstream, which covers the rest of the region in which recombination occurs.

or temperature can greatly effect the rate. Using the rate taken from Mill's data and assuming that the electron temperature and density upstream scale to the electron temperature and density downstream the same way that the upstream and downstream argon temperature and density scale, produces a rate in the range of $10^5 \sim 10^6\ s^{-1}$. Constant recombination rates in this range narrow the ion density profiles sufficiently to produce the downstream profiles. Applying a recombination rate of $4 \times 10^5\ s^{-1}$ results in a $\sim 85\%$ loss in axial analyte density. A comparable drop can be seen from the upstream electron density measured by Lehn et al.(27) to the downstream electron density measured by Niu and Houk. (26)

Three body recombination does not depend on ionization energies, therefore barium and calcium should have the same recombination rates. However, when they are recombined at the same rate, diffusion alone accounts for a 10% difference in calcium and barium profile widths, whereas Ma's data show a 30% difference. Adding the effect of an ambipolar field can account for the

additional width difference. The ambipolar electric field **E** is estimated using:(15)

$$\mathbf{E} = -\frac{1}{en_e}\nabla k_B n_e T_e \approx -\frac{1}{en_0}\nabla k_B n_0 T_e$$

where n_e is the electron density, n_0 is the argon neutral density, e is the elementary charge, k_B is Boltzmann's constant, and T_e is the electron temperature. Four different ambipolar fields are used in FENIX. They are estimated by using two different electron temperatures and two different densities. One electron temperature estimate is 2500 K, the temperature predicted by the three body recombination rate and Mill's data. The other is the electron temperature found by Farnsworth et al.(15) that best matched the observed ambipolar field effects. This temperature starts around 7000 K near the sampling cone and decreases to 3000 K by 10 mm downstream from the sampling cone. The electron density is estimated by either assuming that it is directly proportional to the argon neutral density, or by narrowing the argon density by the same differential quenching that was applied to the trace ion densities, since the electron density should decrease due to recombination at the same rate as the ion densities. The approximated fields are then loaded into FENIX and allowed to affect the trajectory of the trace particles. The results are presented in Fig. 3.5.

Ambipolar diffusion in ProfileMapper is more complex than the ProfileMapper presented here. The ambipolar diffusion coefficient for analyte entrained in the argon involves solving coupled differential equations for the analyte and the argon ion densities and is beyond the scope of this thesis. But, FENIX simulates ambipolar effects correctly.

Once recombination and ambipolar effects are added, FENIX matches Ma's data within the zone of silence. They disagree, however, in the barrel shock. At 10 mm downstream, the shock begins to form at a radius 2-3 mm and is fully formed by 4-5 mm. The outer edge of the simulated FENIX data goes to zero at large radius, whereas Ma's data shows a non-zero leveling out of the analyte in this region. Loading FENIX with wider upstream profiles and turning off recombination does not predict this analyte "floor" seen by Ma. The upstream profiles that would reproduce it must have a much wider density distribution than those measured by Mills. At 10 mm downstream,

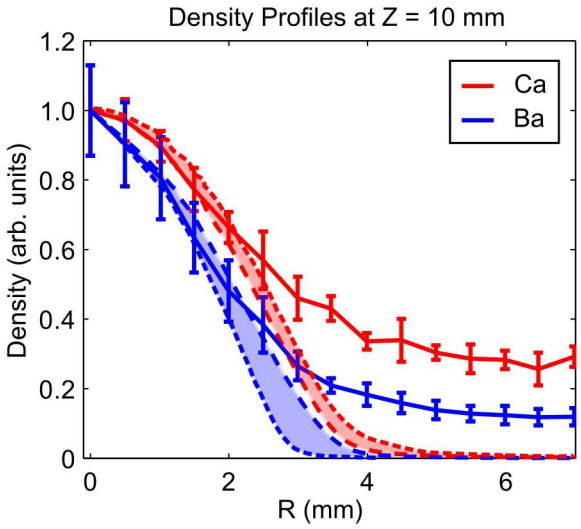

Figure 3.5 Results produced by FENIX compared to Ma's downstream data. — is the experimental data. – – is the results produced by FENIX when using a constant upstream recombination coefficient of $5 \times 10^5\ s^{-1}$ and a small ambipolar field, produced by using $T_e = 2500K$ and using the argon density. - - - is the results produced by FENIX using an upstream recombination rate of $10^6\ s^{-1}$ and a larger ambipolar field, produced a T_e that starts at 7000 K near the sampling cone and decreases to 3000 K (see Farnsworth et al.(15)) and an argon ion density, which is narrowed. The shaded regions show the profile width range that can be reasonably produced by FENIX. The electron temperature that best fits the data should be around 4000 K $\sim$ 5000 K.

in the region where FENIX and Ma disagree (R $>$ 3 mm), the argon temperature climbs from $\sim$500 K to $\sim$3500 K, therefore re-ionization in the shock cone is a possible explanation for the high signal seen by Ma. However, the rate predicted by classical ionization(29) is much too slow to account for this effect. Some other ionization process must be the cause. Another possible cause for this floor is turbulent mixing. The Reynolds number in this region is only $\sim$ 800, which is well below the turbulent regime; however, flaws in the nozzle could seed turbulence. Seeded turbulence would only appear in a full three-dimensional argon flow simulation, which is impractical to do with FENIX.

Chapter 4

Conclusion

Two separate models of analyte flow have been created: FENIX, a DSMC simulation; and ProfileMapper, a continuity equation solver. The models agree with barium data that was taken in the upstream region. The models were also able to show that diffusion is the cause of the previously unexplained drop in the on axis barium ion density.

Also, FENIX and ProfileMapper agree with each other when simulating the region from 0.7 mm upstream from the sampling cone to 10 mm downstream from the sampling cone. However, these convection and diffusion only models disagree with the experimental data in three ways.

First, the calculated density profiles are too wide. Due to travel time effects, adding electron ion recombination in the region from 0.7 mm upstream of the sampling cone to the sampling cone tip, at a rate comparable to what can be calculated downstream from the sampling cone, narrows the density profiles sufficiently to match the experimental data.

Second, standard diffusion alone predicts a much smaller mass dependent difference in profile widths than what is seen in the experimental data. This mass dependent spreading can be accounted for by including estimated ambipolar fields downstream from the sampling cone.

Third, the theoretical profiles go to zero at a large radius, and the experimental data go to a small but non zero value at large radius. This extra effect has not been successfully simulated, and

its cause is unknown.

Bibliography

[1] P. L. Owen and C. K. Thornhill, "The flow in an axially-symmetric supersonic jet from a nearly-sonic orifice into a vacuum," Aeronautical Research Council Reports and Memoranda (1948).

[2] H. Ashkenas and F. S. Sherman, "Structure and utilization of supersonic free jets in low density wind tunnels," in *4th RGD* (1966), Vol. 2, p. 784.

[3] J. W. Brook and R. A. Oman, in *IVth Symposium of Rarefied Gas Dynamics*, J. M. de Leeuw, ed., (Academic, New York, 1965), Vol. 1, p. 129.

[4] P. L. Bhatnagar, E. P. Gross, and M. Krook, "A Model for Collision Processes in Gases. I. Small Amplitude Processes in Charged and Neutral One-Component Systems," Phys. Rev. **94,** 511–525 (1954).

[5] B. B. Hamel and D. R. Willis, "Kinetic Theory of Source Flow Expansion with Application to the Free Jet," Physics of Fluids **9,** 829–841 (1966).

[6] E. L. Knuth and S. S. Fisher, "Low-Temperature Viscosity Cross Sections Measured in a Supersonic Argon Beam," The Journal of Chemical Physics **48,** 1674–1684 (1968).

[7] D. Miller and R. Andres, *VIth Symposium of Rarefied Gas Dynamics* (1969), Vol. 2, p. 1385.

[8] J. P. Toennies and K. Winkelmann, "Theoretical studies of highly expanded free jets: Influence of quantum effects and a realistic intermolecular potential," The Journal of Chemical Physics **66,** 3965–3979 (1977).

[9] A. Kantrowitz and J. Grey, "A High Intensity Source for the Molecular Beam. Part I. Theoretical," Review of Scientific Instruments **22,** 328–332 (1951).

[10] G. B. Kistiakowsky and W. P. Slichter, "A High Intensity Source for the Molecular Beam. Part II. Experimental," Review of Scientific Instruments **22,** 333–337 (1951).

[11] W. Somers, Master's thesis, Brigham Young University, 2008.

[12] D. Douglas, in *Analytical Atomic Spectrometry*, 2nd ed., A. Monaster and D. Golightly, eds., (VCH, New York, 1991).

[13] D. J. Douglas and J. B. French, "Gas dynamics of the inductively coupled plasma mass spectrometry interface," J. Anal. At. Spectrom. **3,** 743–747 (1988).

[14] R. L. Spencer, J. Krogel, J. Palmer, A. Payne, A. Sampson, W. Somers, and C. N. Woods, "Modeling the gas flow upstream and in the sampling nozzle of the inductively coupled plasma mass spectrometer via the Direct Simulation Monte Carlo algorithm," Spectrochimica Acta Part B: Atomic Spectroscopy **64,** 215–221 (2009).

[15] P. B. Farnsworth, R. L. Spencer, W. N. Radicic, N. Taylor, J. Macedone, and H. Ma, "A comparison of ion and atom behavior in the first stage of an inductively coupled plasma mass spectrometer vacuum interface: Evidence of the effect of an ambipolar electric field," Spectrochimica Acta Part B: Atomic Spectroscopy **64,** 905 – 910 (2009).

[16] R. L. Spencer, N. Taylor, and P. B. Farnsworth, "Comparison of calculated and experimental flow velocities upstream from the sampling cone of an inductively coupled plasma mass spectrometer," Spectrochimica Acta Part B: Atomic Spectroscopy **64,** 921 – 924 (2009).

[17] A. A. Mills, J. H. Macedone, and P. B. Farnsworth, "High resolution imaging of barium ions and atoms near the sampling cone of an inductively coupled plasma mass spectrometer," Spectrochimica Acta Part B: Atomic Spectroscopy **61,** 1039 – 1049 (2006).

[18] H. Ma, Ph.D. thesis, Brigham Young University, 2009.

[19] G. Bird, *Molecular gas dynamics and the direct simulation of gas flows* (Clarendon Press, Oxford, 1994).

[20] K. Koura and H. Matsumoto, "Variable soft sphere molecular model for inverse-power-law or Lennard-Jones potential," Physics of Fluids A: Fluid Dynamics **3,** 2459–2465 (1991).

[21] K. Koura and H. Matsumoto, "Variable soft sphere molecular model for air species," Physics of Fluids A: Fluid Dynamics **4,** 1083–1085 (1992).

[22] H. Ellis, R. Pai, E. McDaniel, E. Mason, and L. Viehland, "Transport properties of gaseous ions over a wide energy range," Atomic Data and Nuclear Data Tables **17,** 177 – 210 (1976).

[23] H. Ellis, E. McDaniel, D. Albritton, L. Viehland, S. Lin, and E. Mason, "Transport properties of gaseous ions over a wide energy range. Part II," Atomic Data and Nuclear Data Tables **22,** 179 – 217 (1978).

[24] H. Ellis, M. Thackston, E. McDaniel, and E. Mason, "Transport properties of gaseous ions over a wide energy range. Part III," Atomic Data and Nuclear Data Tables **31,** 113 – 151 (1984).

[25] L. Viehland and E. Mason, "Transport Properties of Gaseous Ions over a Wide Energy Range, IV," Atomic Data and Nuclear Data Tables **60,** 37 – 95 (1995).

[26] H. Niu and R. Houk, "Langmuir probe measurements of the ion extraction process in inductively coupled plasma mass spectrometry-I. spatially resolved determination of electron

density and electron temperature," Spectrochimica Acta Part B: Atomic Spectroscopy **49,** 1283 – 1303 (1994).

[27] G. Gamez, S. A. Lehn, M. Huang, and G. M. Hieftje, "Effect of mass spectrometric sampling interface on the fundamental parameters of an inductively coupled plasma as a function of its operating conditions: Part II. Central-gas flow rate and sampling depth," Spectrochimica Acta Part B: Atomic Spectroscopy **62,** 370 – 377 (2007).

[28] J. H. Macedone and P. B. Farnsworth, "Changes in plasma composition during the expansion into the first vacuum stage of an inductively coupled plasma mass spectrometer," Spectrochimica Acta Part B: Atomic Spectroscopy **61,** 1031 – 1038 (2006).

[29] J. D. Huba, "Naval Research Laboratory Plasma Formulary, revised," (2011).